

Design, simulation, testing and application of laser-sintered conformal lattice structures on component level

David Marschall

Institute of Structural Lightweight Design, Christian Doppler Laboratory for Structural Strength Control,
Johannes Kepler University Linz, Linz, Austria and KTM E-TECHNOLOGIES GmbH, Anif, Austria

Sigfrid-Laurin Sindinger

Institute of Structural Lightweight Design, Christian Doppler Laboratory for Structural Strength Control,
Johannes Kepler University Linz, Linz, Austria

Herbert Rippl and Maria Bartosova

KTM E-TECHNOLOGIES GmbH, Anif, Austria, and

Martin Schagerl

Institute of Structural Lightweight Design, Christian Doppler Laboratory for Structural Strength Control,
Johannes Kepler University Linz, Linz, Austria

Abstract

Purpose – Laser sintering of polyamide lattice-based lightweight fairing components for subsequent racetrack testing requires a high quality and a reliable design. Hence, the purpose of this study was to develop a design methodology for such additively manufactured prototypes, considering efficient generation and structural simulation of boundary conformal non-periodic lattices, optimization of production parameters as well as experimental validation.

Design/methodology/approach – Multi-curved, sandwich structure-based demonstrators were designed, simulated and experimentally tested with boundary conformal lattice cells. The demonstrator's non-periodic lattice cells were simplified by forward homogenization processes. To represent the stiffness of the top and bottom face sheet, constant isotropic and mapped transversely isotropic simulation approaches were compared. The dimensional accuracy of lattice cells and demonstrators were measured with a gauge caliper and a three-dimensional scanning system. The optimized process parameters for lattice structures were transferred onto a large volume laser sintering system. The stiffness of each finite element analysis was verified by an experimental test setup including a digital image correlation system.

Findings – The stiffness prediction of the mapped was superior to the constant approach and underestimated the test results with –6.5%. Using a full scale fairing the applicability of the development process was successfully demonstrated.

Originality/value – The design approach elaborated in this research covers aspects from efficient geometry generation over structural simulation to experimental testing of produced parts. This methodology is not only relevant in the context of motor sports but is transferrable for all additively manufactured large scale components featuring a complex lattice sub-structure and is, therefore, relevant across industries.

Keywords Non-periodic lattice, Multi-scale simulation, Additive manufacturing, Component testing, Lightweight design

Paper type Research paper

1. Introduction

Lattice structures deliver a high bending stiffness to weight ratio and, therefore, are suited well for lightweight structures (Gibson and Ashby, 1999). Rosen (2007) introduced the potential of the design method for additive manufacturing using a slightly curved plate filled with a boundary conformal lattice structure as demonstrator.

© David Marschall, Sigfrid-Laurin Sindinger, Herbert Rippl Maria Bartosova and Martin Schagerl. Published by Emerald Publishing Limited. This article is published under the Creative Commons Attribution (CC BY 4.0) licence. Anyone may reproduce, distribute, translate and create derivative works of this article (for both commercial and non-commercial purposes), subject to full attribution to the original publication and authors. The full terms of this licence may be seen at <http://creativecommons.org/licences/by/4.0/legalcode>.

The financial support by the Christian Doppler Research Association, the Austrian Federal Ministry for Digital and Economic Affairs, and the National Foundation for Research, Technology, and Development is gratefully acknowledged. The authors are also grateful to KTM E-TECHNOLOGIES GmbH for the manufacturing of the test specimens.

Received 2 October 2020
Revised 24 March 2021
Accepted 9 May 2021

The current issue and full text archive of this journal is available on Emerald Insight at: <https://www.emerald.com/insight/1355-2546.htm>



Rapid Prototyping Journal
27/11 (2021) 43–57
Emerald Publishing Limited [ISSN 1355-2546]
[DOI 10.1108/RPJ-10-2020-0232]

Gorguluarslan *et al.* (2015) disclosed that the layer-based additive manufacturing process diminishes the dimensional accuracy of the strut diameters over the strut angle and its corresponding young modulus. According to Maconachie *et al.* (2019), adjustment of process parameters in selective laser melting can yield manufacturable and dimensionally accurate struts with low surface roughness. Breuninger *et al.* (2012) revealed that Young's modulus depends on the wall thickness in laser sintered polyamide. The test specimen thicknesses were 1, 5 and 8 mm. Determination of mechanical properties of thin-walled structures near the laser sintering (LS) system's laser spot size revealed a drastic drop in mechanical performance below coupon thicknesses of 0.8 mm (Tasch *et al.*, 2018). In addition, Sindinger *et al.* (2020, 2021a) demonstrated that in laser-sintered materials the degree of anisotropy in the structural response of tensile coupons is dependent on wall thickness. The influence of the process parameters to mechanical properties for laser sintered polyamides was presented by Caulfield *et al.* (2007). Moreover, the mechanical properties are influenced by the position in the build area of LS system as shown by Goodridge *et al.* (2012) and Tasch *et al.* (2018).

Feng *et al.* (2018) gave a review of modeling approaches for components with lattice structures and design methods for complex topology optimized parts for additive manufacturing. They concluded that optimized components yield a vast potential for lightweight design in actual engineering situations. However, complex demonstrators resulted in very time-consuming finite element analyses (FEA). One of the key time driver on the final FEA results was the direct influence of the meshing process. Boundary conformal design of soft lattice structures on specimen level, its simulation and testing was carried out by Weeger *et al.* (2019). The design approach was extended to a nearly 200 mm big midsole demonstrator of a shoe with an optimized lattice structure. The simulation approach was not validated with testing on the fabricated part. Lynch *et al.* (2018) optimized a demonstrator based on a simple geometry with an asymptotic homogenization approach. To proof the accuracy of the numeric method they used continuum elements and symmetries to cope with the high number of elements. They tested the demonstrator and compared initial failure to FEA results. However, using this approach the numerical effort for large scale lightweight structures would be very high and, therefore, not appropriate for industrial use. Park and Rosen (2018) compared homogenization approaches for strut based lattice structures, accounting for AM process derived effects and joint stiffening. However, it was limited to periodic structures and truss-based cells. In Marschall *et al.* (2020), a forward homogenization (FH) process was proposed to capture the stiffness and initial failure of surface- and strut-based lattices. However, the finite element (FE) approach was validated only on periodic and orthogonal three point bending test coupons. This FH approach for lattices was used in the present study to evaluate its performance in an engineering situation on a demonstrator level. Further objectives of the FE model investigation were the element size distribution, lattice cell distribution and mesh quality as well as the connection of the solids with the lattice models.

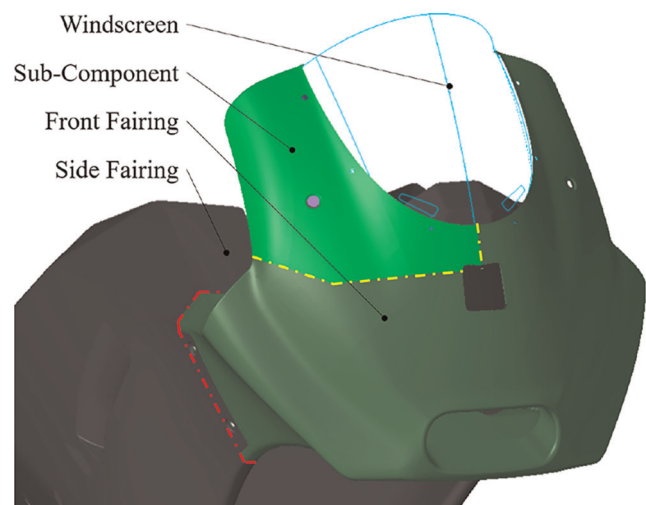
A sub-component consisting of a front fairing segment (Sub-FF) was used as complex demonstrator to evaluate the stiffness prediction of two FE approaches, featuring a FH

process. The stiffness and shape of a lattice filled sandwich structure used in racing motorcycles, such as the Sub-FF, needs to meet safety, aerodynamic, rider ergonomic and riding style demands. Aerodynamically relevant and FE analysis-derived components, such as the motorcycle fairing shown in Figure 1, can be mounted immediately after the additive manufacturing process and assessed regarding their racing performance on the racetrack. However, an upfront FEA only makes sense, if the LS system can deliver continuity in terms of material properties on a demonstrator level. The knowledge of the system-specific Young's modulus and material properties of lattice structures and its possible defects need to be taken into account for FEA.

Another field of investigation of this paper was, how to efficiently remove the powder from sandwich structures like the Sub-FF, where most of the surface needs to be closed due to aerodynamic reasons. Powder removal is essential as accumulated residues would influence the component mass and affect the structural response of lattice trusses.

The process stability and the influence of process parameters on thin-walled shell structures and struts close to the smallest achievable feature size were taken into account. Therefore, a process parameter optimization for LS PA12 lattice structures was conducted as presented in subsection 2.1.2. The used demonstrators were evaluated regarding memory space, production effort, reliability and weight. The knowledge gained from the presented FE approach and production investigation was subsequently transferred from the Sub-FF to two complete fairing demonstrators. An assembly consisting of a large-scale front fairing (FF-L) $587 \times 476 \times 414 \text{ mm}^3$ ($L \times W \times H$) and a windscreen (Figure 1) was used for a modal analysis with boundary conditions. Thereby, it was important that the first mode was not introduced by the lattice structure itself. Resonant excitation of the fairing arising from low frequency vibrations

Figure 1 Assembly of a racing motorcycle fairing



Note: Entire front fairing with highlighted sub-component for demonstrator purposes, side fairing and windscreen

below 40 Hz that typically occur during racing, impedes functionality and can ultimately lead to failure of the component.

For reasons of cost efficiency, a medium-sized front fairing (FF-M) was chosen for a manufacturability and mounting study. With a size of $563 \times 519 \times 227 \text{ mm}^3$, the FF-M used up almost the entire build space of the LS system during fabrication. This step was essential to evaluate the dimensional accuracy of the LS process for customized motor sport fairings. Overall, the aim of the study was to validate the design process for large scale additively manufactured polyamide 12 components considering FEA and manufacturability.

2. Methodology








2.1 Lattice parameter optimization

As aforementioned, the potential of lattice structures for lightweight design can be diminished by geometrical deviations that may arise from characteristics of the layer-wise manufacturing process. Hence, to fabricate dimensionally accurate lattice truss diameters, a parameter optimization was conducted.

2.1.1 Design of the lattice cuboid

Based on the three-point bending (3PB) test specimens from Marshall *et al.* (2020), a representative cuboid section was considered for the parameter optimization. The dimensions of the lattice cuboid were defined as $21.42 \times 21 \times 20 \text{ mm}^3$, featuring constant truss thicknesses of 0.8 mm. The top and the bottom face sheet wall thicknesses were set to 0.8 mm as well. Each unit cell measured $7.14 \times 7 \times 6.13 \text{ mm}^3$ leading to 27 cells in the sandwich cuboid. The cells adjacent to the closed faces were of type simple cubic body-centred cubic (sc-bcc), while the middle ones were face-centred cubic (fcc). The respective unit cell types are displayed in Figure 2. Figure 3 exhibits the two produced cuboid orientations, whereby the *S*, *L* and *X* marks indicate short horizontal, long vertical and cross truss beams, respectively that were used for evaluation of the parameter study

Figure 2 Proportion of RVE of Sub-FF

	UC	dimensions in mm		
		x	y	z
	bcc I	4.6	5.9	8.6
	bcc II	4.6	5.5	6.5
	bcc III	4.6	4.8	5.3
	sc-bcc I	4.6	6.2	8.2
	sc-bcc II	4.6	5.5	6.8
	sc-bcc III	4.6	4.8	5.3
	sP	4.6	5.2	5.6

(see subsection 2.1.2). Consideration of the two variants yields insights into the effects of the process parameters in global coordinate system aligned and arbitrarily oriented lattices.

2.1.2 Production, parameter variation and measurement of the lattice cuboid

An iterative parameter optimization was performed using a trial and error process. A total of four build jobs were built, three in an EOS P396 (Munich, Germany) and one final job in a larger and more expensive EOS P770. The smaller P396 machine was used mainly to avoid the substantially higher build job costs on the P770. In the P396, PA12 sintering powder from EOS (PA 2200) was mixed at a ratio of 50% virgin and 50% aged material. Due to cost efficiency a ratio of 40% virgin and 60% aged PA, 2200 powders was mixed for the P770.

For the parameter optimization laser power (W) and scan speed (mm/s) of the contour and edge parameters detailed in Tasch *et al.* (2018) were manipulated as variables. The scan spacing (mm) and hatch pattern were kept constant at default level. Further, the laser contour offset (mm) was varied. Finally, the z-compensation (mm) and angle-based z-compensation (mm), which are correction values for characteristic geometrical deviations in vertical (z) and additional angled directions, were manipulated. The powder layer thickness during the manufacturing process was always the same and amounted to 0.12 mm.

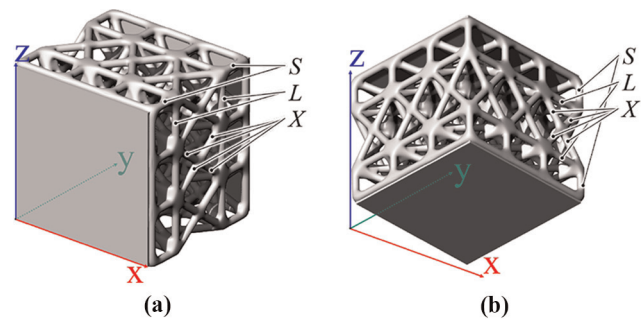
The truss diameters of the test specimens were measured with a caliper on the *S*, *L* and *X* beams all around the four open cuboid faces (Figure 3). The mean value of the \bar{S} -, \bar{L} - and \bar{X} -diameters was then used for the parameter evaluation.

To minimize differences arising from specific build positions, the cubes were randomly distributed in the build area in all build jobs. The test specimens were investigated as-built without any further finishing process.

Initially, the default parameter set was used as base for the variation. The magnitude of variation in each parameter was determined by the know-how of the industrial machine technician. This approach does not yield a broad screening of parameter correlations like other design of experiments approaches but rendered more efficient for the present aim to improve dimensional accuracy of lattice truss diameters.

In the first and second build job the lattice cuboids were produced in an upright orientation [Figure 3(a)], with the closed

Figure 3 Lattice cuboid for parameter investigation with *S*-trusses, *L*-trusses and *X*-trusses for diameter measurement



Notes: (a) Upright orientation; (b) 45° rotated orientation

surfaces in the xz -orientation. The parameters that resulted in the smallest deviations in dimensional accuracy of the truss diameters per job were subsequently transferred to the next job and varied again. To investigate the influence of the parameter sets for arbitrary lattice orientations, the cuboid was rotated by 45° of all three axes [Figure 3(b)] in the third build job. The results generated were then transferred to the final build job in the P770. The default parameter set of the P770 was used as a base and then varied with the parameters that were previously identified to contribute to dimensional accuracy. Transferability between machines was assumed due to the fact that they solely vary in terms of available build volume and number of lasers.

2.2 Design, finite element analysis and test setup on sub-component level

2.2.1 Design of core, top and bottom face sheet

The lattice design process of Marshall *et al.* (2020) was applied on the geometry of the Sub-FF. Consequently, at least three solid CAD geometries were required to model the Sub-FF: top and bottom face sheet as well as the core. To create rigid sandwich structures, solid bottom and top face sheets and a stable core structure are needed. The step-wise design process is presented from bottom to top face sheet in Figure 4.

The basis of the Sub-FF design is a generically designed core, discretized in HyperMeshTM 2020 (Altair Engineering, Inc., Troy, USA) using second order elements. The latter were used despite the increased computational cost compared to first order elements, as the additional node and quadratic shape function enables the unit cell trusses to be curved, which results in superior boundary conformity. While efforts were made to mesh the entire core of the Sub-FF with periodical orderly structured rectangles (Hex20), due to geometric complexity of the part, also distorted hexahedrons and a marginal amount of pentahedron elements (Penta15) were required, as seen in Figure 4(a).

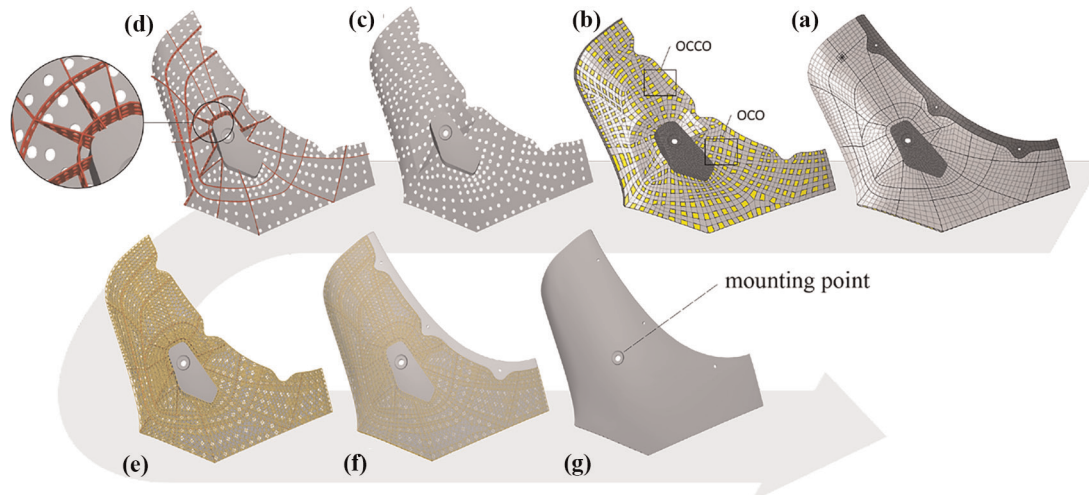
To enable a full-area powder release, it was necessary to provide a sufficient number of holes in the bottom face sheet. The hole pattern depends on the core mesh and was likewise derived in HyperMeshTM. As indicated in Figure 4(b), two

different hole patterns were used to allow powder removal in the subsequent cleaning process. In regions where powder removal is impeded by usage of sP surface-based cells and increased relative lattice density (see next paragraph), an alternating open-closed-open (OCO) pattern was applied. Where lattice density was lower and truss-based unit cells facilitated powder removal an open-closed-closed-open (OCCO) configuration was seen as sufficient. Figure 4(c) depicts the bottom face sheet with the integrated holes.

To take up compression stresses as a consequence of handling during mounting and aerodynamic loads on a FF, a generic stringer design was introduced into the lattice core. These stiffeners are shown in Figure 4(d), were 0.8 mm thick and were implemented using Grasshopper®, a visual programming tool for generative design within the software Rhinoceros® (Robert McNeel & Associates, Seattle, USA). One hole per element was modeled, whereby the hole size was dependent on the element size. The holes were introduced into the stringer to save weight and to ensure powder removal. The additional load stringers enclosed the lattice structures.

The FE mesh constitutes the basic framework of the lattice structure [Figure 4(e)]. The mesh-based lattice generation was performed using Dendro (ERC LABS LLC, Los Angeles, USA), an open-source Grasshopper® plug-in. When designing the core of the Sub-FF, its similarities to a basic cantilever beam should be considered. As the bending moment increases toward the mounting point, a higher moment of inertia is required in this region to achieve a rigid structure. Therefore, the element size was decreased and the number of elements increased in the mounting point area. The diameter of the truss beams and the wall thickness of the surfaces was independent of lattice cell size and remained constant at 0.8 mm in the present approach. Smaller lattice cells with the same beam diameter have a higher relative density and thus a higher stiffness. This also reduces the length of the lattice beam and thus the susceptibility of these beam to buckling. In the cross-section around the mounting area the number of core elements was increased from one lattice cell element to three lattice cell

Figure 4 Design process with solid core mesh (a), powder removal hole pattern (b), perforated bottom face sheet (c), stringer topology (d), boundary conformal lattice core (e), combination of cellular structure with functional solid regions (f) and final Sub-FF including the top face sheet (g)



elements; therefore, the distance between the outer sheets and the neutral fiber was increased.

Finally, the bottom face sheet, the stringers and the lattice core were merged together with functional solid structures such as the mounting region of windscreen [Figure 4(f)] and the fully closed top face sheet that functions as aerodynamic guidance [Figure 4(g)]. The combination of the separately existing parts and conversion to Standard Triangle Language (STL) for production ready output was performed in Grasshopper® as well.

2.2.2 Numerical investigation

The focus of the investigation of the Sub-FF was the stiffness evaluation with macro-homogeneous linear material properties. These were obtained using an FH approach detailed by Marschall et al. (2020), where virtual loading of unit lattice cells yields the effective homogenized stiffness tensor that allows efficient representation of lattices via solid elements, instead of complex networks of trusses and void volumina. The commercial software packages used for the FH of a unit cell (UC) were Multiscale Designer™ 3.4 (MSD) and Hyperworks OptiStruct™ 2019 (Altair, Troy, United States). A virtual test setup in a numerically efficient FE analysis model was solved using OptiStruct™ to obtain the force-displacement-curve based on the stiffness of the Sub-FF.

For the geometric non-linear simulation, the complete discretization approach regarding the mesh and two material modeling approaches for the surfaces (FEA C) and FEA M are presented in Figure 5. The solid geometry in the mounting area

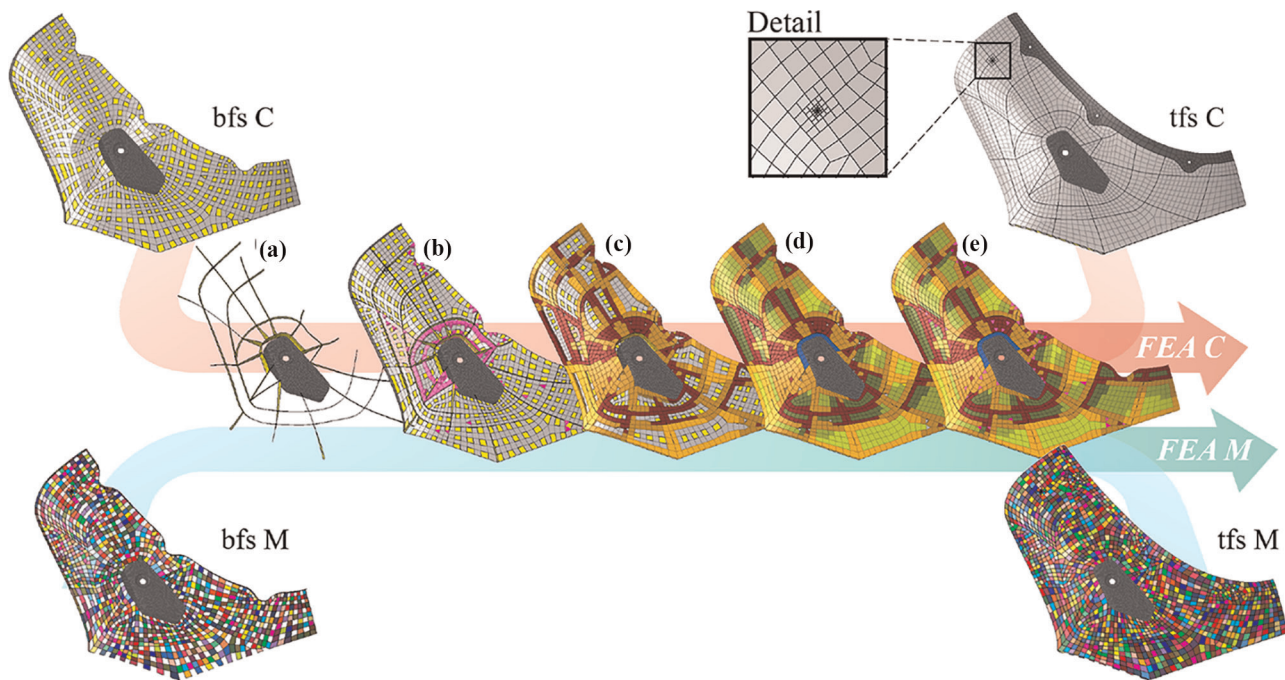
was discretized using unstructured second-order tetrahedron (Tet10) elements. Its connection to the core elements was implemented with a contact (no sliding and separation capabilities). The nodes of the top and bottom face sheet as well as the stringers were modeled with a coincident element connection to the core node and consisted of first order triangle (Tria3) and quadrilateral (Quad4) elements. The lattice core consisted of second-order hexahedron (Hexa20) and pentahedron (Penta15) elements.

In the first simulation approach (FEA C), for each occurring wall thickness a respective constant material property was defined. The bottom (bfs C) and the top face sheet (tfs C) were 0.8 mm thick. The windscreen mounting surface measured 1.3 and 3 mm. The stiffnesses of these structures were deduced from material properties reported by Tasch et al. (2018), based on 0.8, 1.2 and 4 mm thick z-oriented tensile test specimens.

In the second simulation approach (FEA M), for bfs and tfs a material modeling concept developed by Sindinger et al. (2021) was used that, dependent on local shell element thickness and orientation, computes and maps material parameters throughout the entire model, based on transversely isotropic (MAT8) material cards. These inhomogeneous material properties are visualized in bfs M and tfs M in Figure 6.

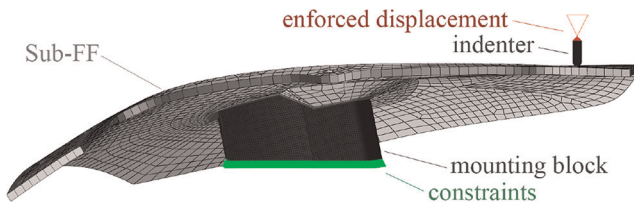
The FH approach (Yuan and Fish, 2008; Fish, 2014), which was in good agreement with the test results for small displacement analyses (Marschall et al., 2020), was used to calculate the macro-homogeneous linear material properties of

Figure 5 Discretization and material modeling approach starting with the bottom face sheet (bfs) and ending with the top face sheet (tfs)



Notes: The bfs and tfs was discretized with thickness depended, constant (FEA C) and mapped with thickness- and angle-depended (FEA M) material properties for each cell. The composition of the core with color scheme according to Figure 2 including stringer elements (a), pentahedron elements in magenta; (b), clustered sc-bcc; (c) bcc and sP hexahedron elements; (d) as well as the complete combined core model; (e). Detail of refined mesh at load introduction

Figure 6 Finite element model representing the experimental load case in subsection 2.2.4



the listed lattice cell types in Figure 2. The FH process provides linear orthotropic elastic properties, which were represented by the MAT90RT material card for numerical investigation via OptiStruct™.

To represent a truss diameter of 0.8 mm, material properties such as the Young's modulus and Poisson's ratio of 0.8 mm thick tensile specimens (Tasch *et al.*, 2018) were used. An increase in the material thickness in the joints, and thus different material properties, was neglected. The material properties of the stringer elements and the elements which represent the powder removal holes were defined with the FH approach, see Figure 5(a). A single representative volume element (RVE) with a wall thickness of 0.8 mm, a representative cell size of 5 mm and a hole size 3 mm was used.

In terms of structural design several cell lattice types were investigated by Marschall *et al.* (2020) and used in different areas of the Sub-FF. All lattice cells (Figure 2) exhibited an anisotropic behavior. Bcc-lattice structures disclosed the highest specific stiffness for 3PB-sandwich beams and therefore, were mainly used throughout the Sub-FF. To achieve an increased pressure stability, the pressure and shear stable Schwarz Primitive (sP) lattice structures, with the highest shear specific value (Marschall *et al.*, 2020), were used for the core elements in the area of load introduction. As transition elements, sc-bcc-cells were used from the sP-lattice structures and stringer elements to the bcc-lattices. Sc-bcc-configurations presented a very good bending stiffness, but also have increased tensile and compression stability compared to the bcc-type. To calculate material stiffness tensors for all different cells with respect to their geometric distortion, it would be necessary to generate 3266 RVE for the Sub-FF, which is not feasible in any realistic time frame.

Hence in this paper, a *k*-Means-algorithm was used to group similar UCs based on their element edge lengths. The goal of this algorithm is to partition a given set of data in *k* clusters, in such a way, that the sum of the squared distances *S* from each data point x_j to its corresponding cluster center μ_i reaches a minimum, as displayed in equation (1):

$$S = \sum_{i=1}^k \sum_{x_j \in C_i} \|x_j - \mu_i\|^2 \rightarrow \min, \quad \mu_i = \frac{1}{|C_i|} \sum_{x_j \in C_i} x_j \quad (1)$$

where C_i is the i^{th} cluster, which have the number of respective members as value (Na *et al.*, 2010). Sorting was based on the edge lengths of the lattice UCs. Therefore, each elements' representative edge lengths $\underline{d} = (x, y, z)^T$ were calculated as the distance between center points of each

opposing face in *x*-, *y*- and *z*-direction of the local elemental coordinate system. To represent elements of similar sizes, but different orientations by the same unit cell, each representative vector (\underline{d}) was sorted according to $z > y > x$. This *de facto* coordinate transformation was then also applied individually to each hexahedral element. For each truss-like cell type (sc-bcc, bcc), a *k*-value of 3 was used, resulting in three RVEs per type as shown in Figure 2. The sP cell was represented by one RVE. While higher *k*-values could lead to a better approximation, the most time consuming process of manually preparing a high amount of homogenized unit cells limited the number of considered clusters in the proposed method, which is intended for application in an industrial context.

This process yields that all core elements have a macro-linear averaged, but nevertheless oriented orthotropic material tensor. In addition, the pentahedron elements were assigned the material property of the adjacent Hex20 cells. The RVE distribution based on the homogenized lattice cells in the core of the Sub-FF is presented in Figure 5(b)–5(e).

As can be deduced from Figure 2, all solid elements of the model were represented by rectangular UCs. Thereby, the actual shape that may deviate from a cuboid and consequently affect the UC's structural response is neglected. This is justified by the fact that in the proposed approach, the lattice is generated based on the mesh, which can be manipulated to avoid highly distorted elements. By performing checks on the minimum and maximum apparent element angles, close to cuboidal lattice UC shapes can be ensured. Depending on the efforts to create a high-quality mesh, the proposed method will yield satisfactory results in most geometries.

Single point constraints for the degrees of freedom 1–6 were applied on the bottom face of the solid mounting block as indicated in Figure 6. The Sub-FF was rigidly bonded to the top face of a machined steel mounting block (Figure 8) via a contact definition, in which degrees of freedom 1–6 were fixed. The enforced displacement load was applied through a indenter and the analysis was conducted for a maximum displacement of 5 mm. The mesh in the contact area of the indenter was refined with smaller elements (Figure 5) for a better contact convergence and the contact conditions were modeled as friction contacts.

2.2.3 Production

The Sub-FFs were produced on three height levels in the build room of the P396. As depicted in Figure 7 the Sub-FFs were oriented horizontally and positioned in 42, 124 and 206 mm *z*-distances from the *xy*-plane of the build envelope.

The parameter setup 3 T, displayed in Figure 10(a), was used for the three Sub-FFs. Furthermore, the Sub-FFs were blasted with glass beads and investigated as-built. To evaluate the influence of the powder removal the Sub-FFs were weighted with a DE6KO.5A (KERN & SOHN GmbH, Frommern, Germany) with a resolution of 0.5 g.

2.2.4 Experimental testing

The dimensional accuracy of the built Sub-FF was measured with a laser scanner, namely, HP-L-20.8 (Hexagon, Stockholm, Sweden). The minimum point density was 0.013 mm and the scanner system accuracy SE was 0.075 mm. The reference region for the dimensional accuracy comparison to the CAD-data was the mounting point.

Figure 7 Sub-FF orientation and position in the build room

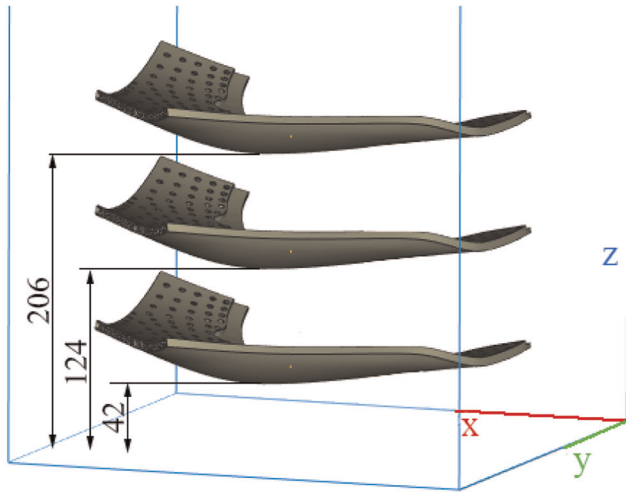
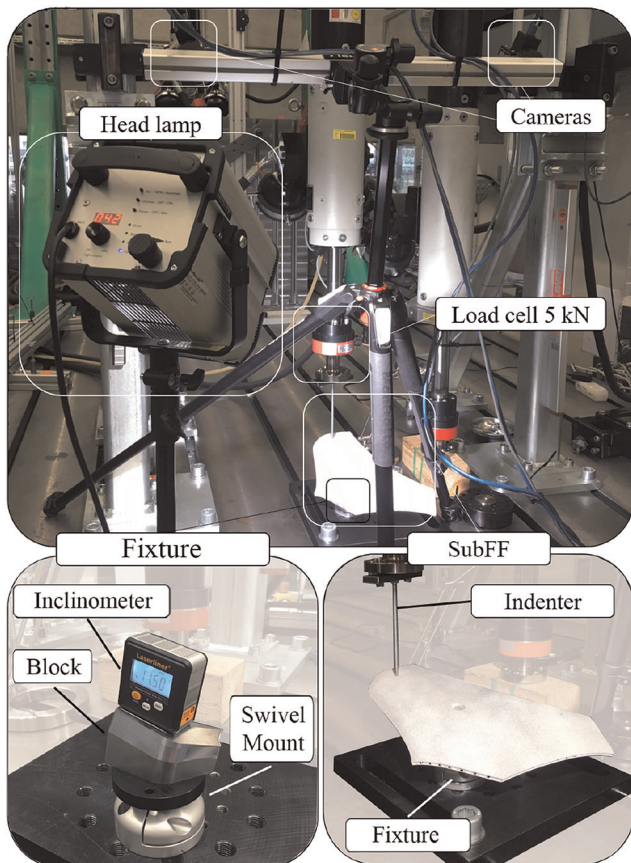


Figure 8 shows the test rig that was used to obtain experimental load-displacement curves of the three Sub-FFs. The tests were performed at room temperature. The Sub-FFs were tested unconditioned. A generic test load case similar to a cantilever beam load case was used to evaluate the stiffness of a Sub-FF. To investigate the accuracy of FE-model and the produced Sub-FF, the mean value of the experimentally determined

Figure 8 Mechanical test setup with DIC on the Sub-FF



force-displacement curves was compared with the simulated ones. The force was measured with a 5 kN load cell. The testing velocity was 1 mm/min. To obtain the stiffness, the traverse displacement value was recorded until 5 mm.

A steel block was machined to represent the geometry of the motorcycle where the fairing is normally attached. This block was placed on a swivel mount that allowed orienting the Sub-FF to match the FE model (Figure 6). For adjustment of the of the correct orientation with respect to the load introduction, an inclinometer was used (Laserliner MasterLevel, UMAREX, Arnsberg, Germany). To ensure permanent contact between test specimen and mounting block during loading, they were glued together using a two component epoxy based adhesive (Loctite EA 9466, Henkel AG & Co. KGaA, Düsseldorf, GER). A digital image correlation (DIC) system (Correlated Solutions, Columbia, USA) was used to evaluate the global and local strain distribution of the Sub-FF at an image capturing rate of 2 Hz.

2.3 Complete component demonstrator

A complete front fairing (FF) was used on the one hand for the numerical effort evaluation with a constrained modal analysis, which was set up using a Normal Modes load step in OptiStruct™ and on the other hand the handling of data resources were monitored. With regard to the FE model, see Figure 9(a), the number of elements and the number of RVE to be calculated is of interest. In terms of production engineering, this refers to the file sizes of the STL data. Furthermore, it shall be investigated whether it is possible to print a FF with a fine lattice structure in the required size dimension on a P770. A laser scan and mounting investigation was carried out to measure the distortion of the additive manufactured FF.

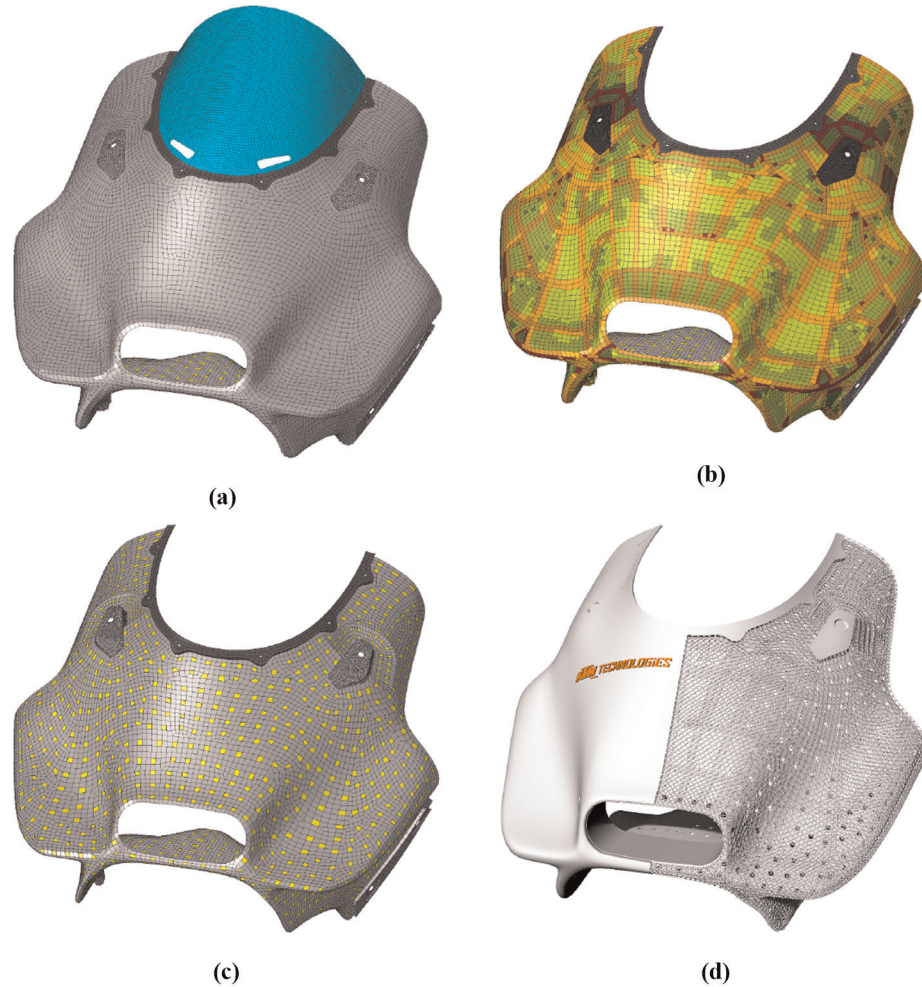
3. Results

3.1 Process parameter optimization and dimensional accuracy

The process parameter optimization from the four sequential build jobs and the corresponding truss diameter results are shown in Figure 10(a) and Figure 10(b), respectively. The first build job shows that the parameter setup 1B with a diameter of 0.55 to 0.9 mm had the smallest deviation from the target value (0.8 mm). The X-trusses of the parameter setup 1B had also the smallest diameter deviation. The parameter setup 1C showed the smallest range of diameter deviations with 0.45 to 0.75 mm on the respective trusses. However, the cross section of the bars was too small. Parameter setup 1E had very small deviations from the nominal value for the \bar{S} - and \bar{L} -trusses. The diameter of the \bar{X} -trusses was comparatively the worst with 0.4 mm.

Based on the parameter setup 1E, the parameter setups 2G and 2H were varied in the second build job. The contour offset (parameter setups 2I to 2K) led to a significant shift in the deviations of the cross trusses to be slightly above the nominal value. This was accompanied by an increase in the diameters of the \bar{S} - and \bar{L} -trusses. A parameter combination of the offset and the angle-based z-combination in parameter setup 2K resulted in L-trusses with 0.78 mm and \bar{X} -trusses with 0.79 mm diameters hitting the nominal value accurately. The z-

Figure 9 FE-model of tfs and windscreen (a), the FH lattice core (b), bfs including holes (c) and production data of the full scale front fairing with a tfs cut out (d)



compensation in parameter setups 2J and 2N resulted in the \bar{L} -Trusses in hitting the nominal value.

In the third build job, the contour offset, z-compensation and angle-based z-compensation were used for all parameters. As a result, the bandwidth of the nominal diameter could be reduced to (± 0.05 mm). By increasing the edge scan speed, parameter setup 3Q for the straight lattice structures and parameter setup 3T for the rotated lattice structures provided with (± 0.01 mm) the smallest deviations from the nominal value in this investigation. With the transfer of parameter setup 3T to P770, parameter setup 4X showed a maximum deviation of 0.03 mm from the nominal value.

Figure 11 shows the scan strategy path as a comparison of parameter setup 1A (default parameter) and parameter setup 3T (parameter with smallest diameter deviation). The default parameter had a very punctiform, nearly overlapping laser path. The thin blue line in Figure 11(a) clearly shows the offsetting – a widening of the contour laser guidance – for the cross trusses. For the \bar{S} -trusses in Figure 11(b), it can be identified that the default parameter has no contour line. Depending on the positioning of the lattice cell in the build area, a horizontal lattice truss has six to seven layers. The main difference

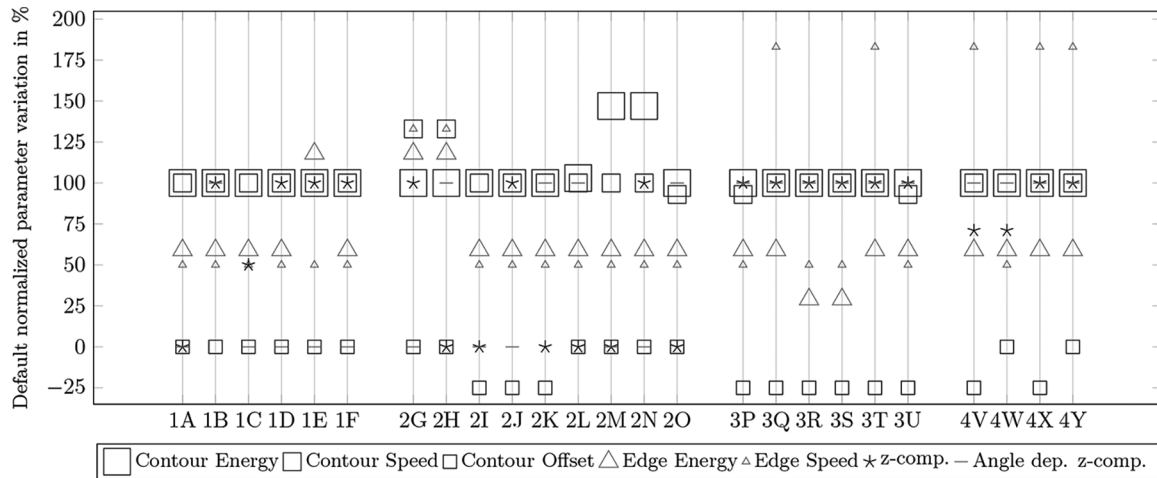
between the default parameter and the 3T parameter setup is that the top and bottom layers of the beam had a higher energy input due to the additional contour path. In the parameter setup 3T, an additional contour-scan was made to the edge-scan. In Figure 11(c) the standard parameter has a very small offset in the contour line compared to the contour parameter. Due to the offset, a broadening of the contour scan similar to Figure 11(a) can be observed. This leads to a less punctual and more homogeneous energy input.

3.2 Evaluation of design, finite element analysis and validation of a sub-component demonstrator

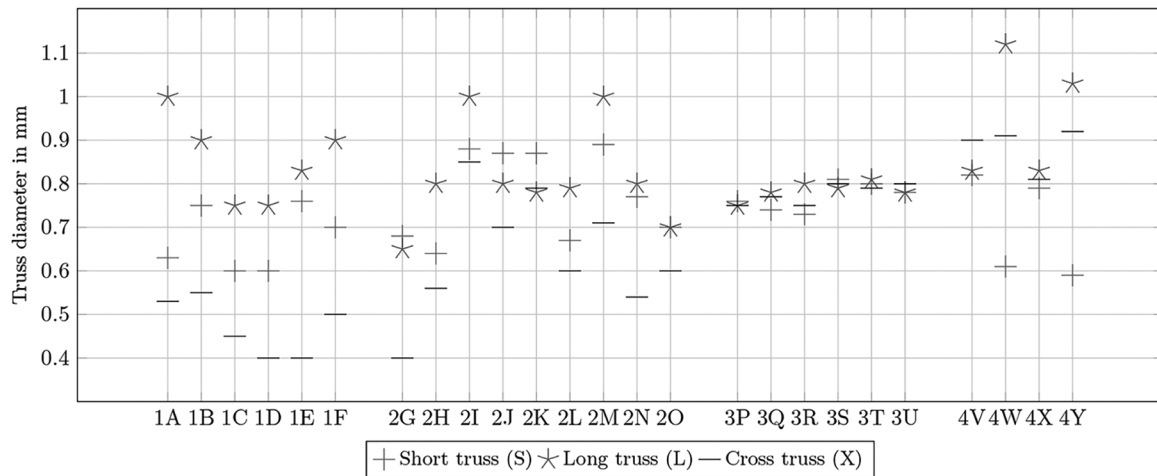
3.2.1 Dimensional accuracy and mass evaluation

For the dimensional accuracy inspection, the clamping surface in the area of the mounting hole served as the reference surface. At the build position of 124 and 206 mm, the Sub-FF showed a tip z-deviation of 3.5 mm, see Figure 12(a) and 12(b). The part fabricated at 206 mm [Figure 12(a)] showed at the medial edge a positive z-deviation of 5 mm. Figure 12(c) illustrates the lowest deviation of approximately 1.5 mm at a build height of 42 mm. The dimensional accuracy of the clamping holes to the mounting holes for the windscreen was in the range of

Figure 10 Parameter optimization



(a)



(b)

Notes: (a) Variation of parameters within four build jobs; (b) measured truss diameter for each parameter set

Figure 11 Comparison of standard (left) and optimized (right) scan strategy for the vertical (a), the beginning planar lattice beams (b) and in the middle section of planar lattice beams (c)

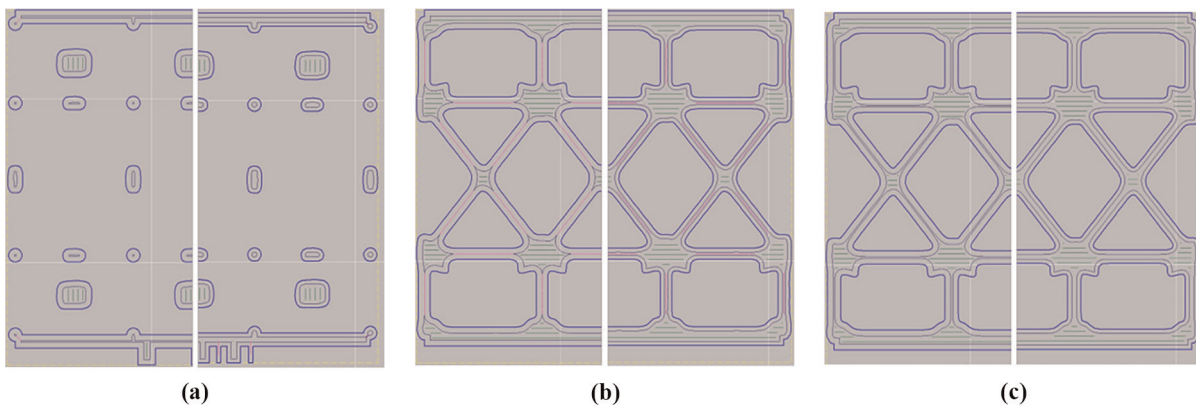
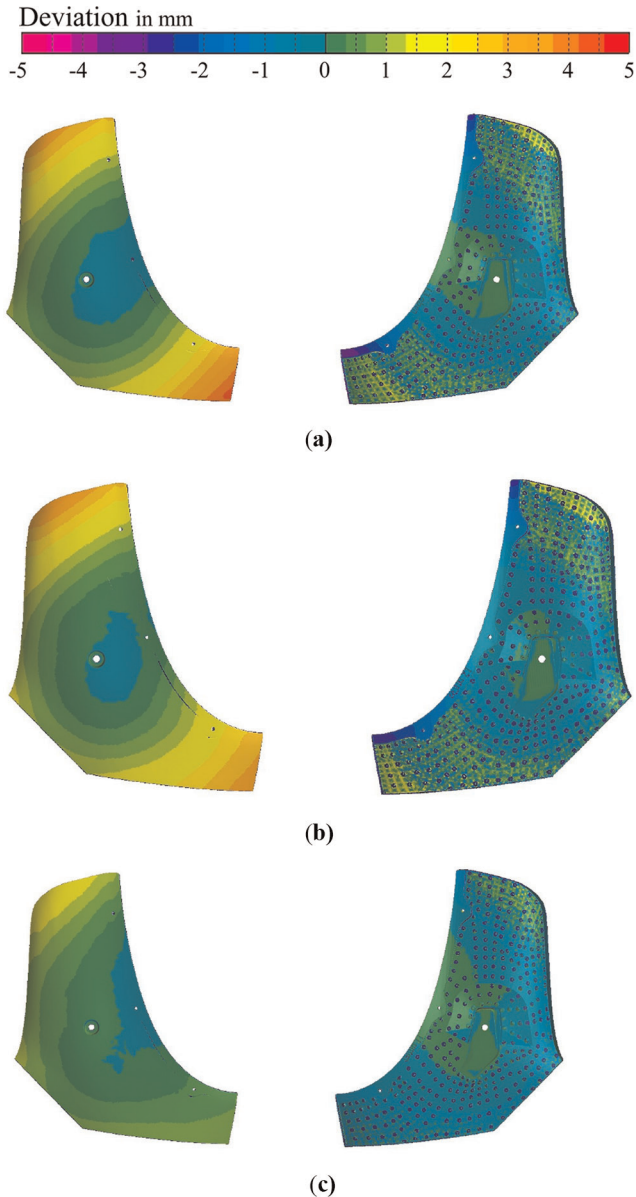


Figure 12 Build deviation to CAD of top and bottom view at top (a), middle (b) and bottom (c) position of LS system

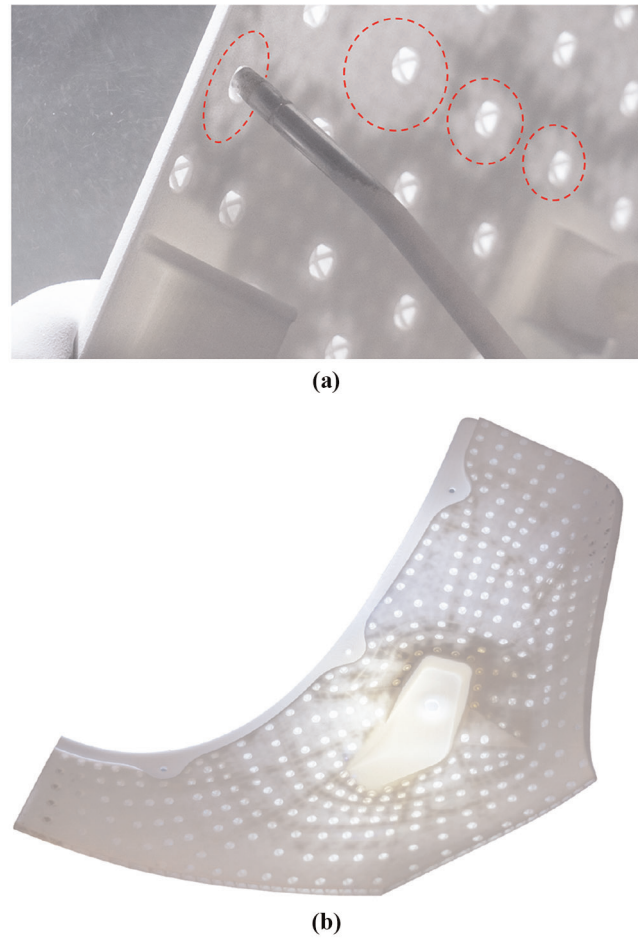


Notes: (a) Build position in z-direction 206 mm; (b) build position in z-direction 124 mm; (c) build position in z-direction 42 mm

± 0.5 mm. The positive deviation at the tip of the Sub-FF was about 2 mm in z-direction.

Figure 13(a) demonstrates the cleaning process by removal of residual powder using pressurized air on the bottom face sheet. In the back-lit image, see Figure 13(b), bright white areas represented powder free areas, yellowish areas showed fully sintered powder and dark gray areas indicated residual powder areas. The bcc-lattice type allowed easy and fast powder removal. Powder removal was most difficult in the clamping area of the sP-lattice type, where there are enclosed unsintered or partially sintered powder residues. The dark gray residues are

Figure 13 Powder removal of the Sub-FF



Notes: (a) Powder removal with pressurized air probe; (b) dark spots with residues of un- or partially sintered powder on Sub-FF

also clearly visible in the areas near the stringers as well as in the clamping area with high relative density of sc-bcc lattice types. If bcc-lattice types are placed under a powder removal hole, the powder can be removed more easily and more extensively within the structure with air pressure than with sc-bcc lattice types.

The mass of the sintered Sub-FF at the 42 mm height position was 143 g, at the 126 mm position it was 144 g and at 206 mm it was 140.5 g. The mean value of the mass was $142.5 \text{ g} \pm 1.8 \text{ g}$, therefore, mass of the produced Sub-FF varies only within $\pm 1.3\%$. The total mass of the simulation model was with 128.9 g 9.6% lighter than the manufactured Sub-FF.

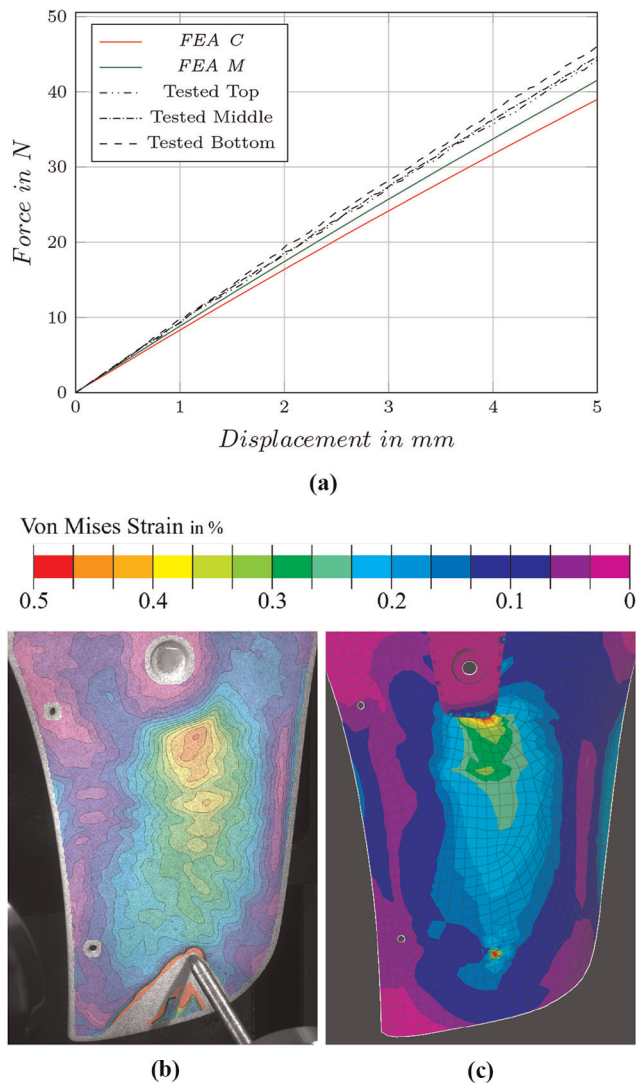
3.2.2 Experimental validation of finite element analysis

Force-displacement curves of the three tested Sub-FFs and the simulation results of the *FEA C* and *FEA M* models are illustrated in Figure 14. The tested mean value at 1 mm indenter displacement was 9.48 N with a coefficient of variance of $\pm 3,0\%$. The highest reaction force with 9.80 N was generated from the Sub-FF at a height position of 42 mm, followed by the height position 124 mm with 9.38 N and 206 mm with 9.26 N. The tested mean value at 5 mm indenter displacement was 45.57 N with a standard deviation of $\pm 3,3\%$. Similarly to the displacement at 1 mm the highest reaction force at 5 mm was

generated from the Sub-FF at a height position of 42 mm with 47.19 N followed by the height position 124 mm with 45.31 N and 206 mm with 44.20 N. The discretization of the *FEA C* model underestimated the test mean value at 1 mm with 8.32 N by 12,2% and at 5 mm with 38.98 N with 14.4%. The *FEA M* model was twice as close to the tested mean value at 1 mm with 8.86 N by 6.5% as the *FEA C* model. The deviation of the *FEA M* model at 5 mm with 41.53 N was only 8.9%.

Figure 14(b) and 14(c) present the tested and calculated von Mises strain at 5 mm displacement. The global strain pattern between FEA and DIC is very similar, but strain in DIC data is higher and more homogeneously distributed between fixture and load introduction. In contrast, in the FEA models there was a sudden increase in strain in the transition between the solid elements of the mounting block and shell elements of the tfs. This localized behavior is attributed to the drastic change in elasticity between the

Figure 14 Force-displacement curve of the two simulation approaches with constant and mapped material properties and the tested Sub-FF (a); Von Mises strain plot of tested Sub-FF (b); and the FEA (c) at 5 mm displacement



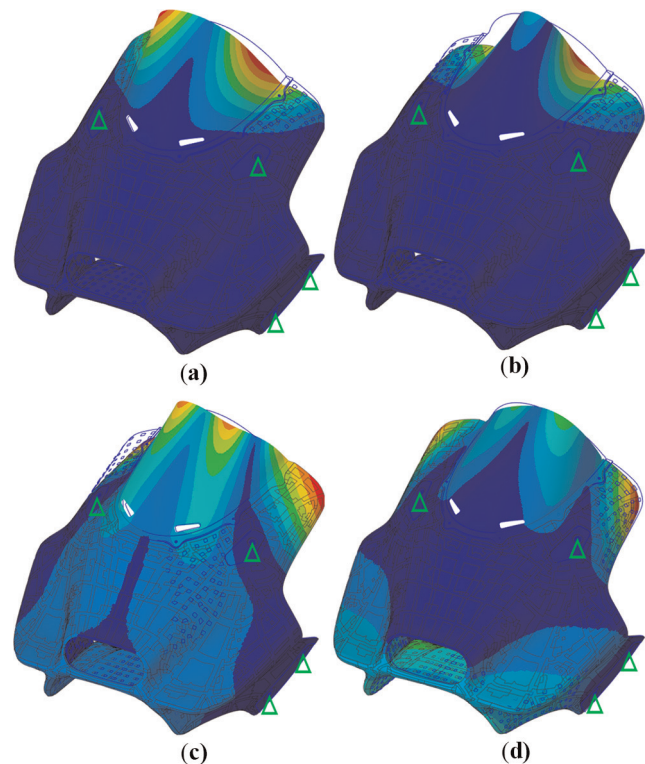
rigidly constrained solid elements of the fixture and the much more elastic shell elements of the remaining part.

3.3 Modal analysis and production of a component demonstrator

Both FF-M and FF-L were modeled with the same approach as the Sub-FF. The constrained modal analysis was an assembly of the FF-L and its windscreen. The structure was constrained in degrees of freedom 1–6 at the locations it is in reality fixed to the motor cycle, namely, the upper mounting points, as well as attachment points on the side and bottom. Figure 15 depicts modes 1–4 as obtained from the numeric simulation for the FF-L as well as the implemented constraints. The lowest frequency (mode 1) amounts to 48 Hz, which indicates that the structure will not resonate as consequence of vibrations introduced by surface irregularities on the road that typically lie well below 40 Hz. The windscreen is excited in mode 1 and 2. At mode 3 the free ends of the FF-L moved reciprocally up and down. Mode 4 indicated a rotational movement around the z-axis of the whole FF-L.

Based on the experience gained in the Sub-FF the splitting of the core in CAD was simplified and the UC size was enlarged. Therefore, the number of pentahedral elements of the FF-L could be reduced from 5% to 2%. Only 11810 elements were required for the lattice core. For the FF-M the percentage of pentahedral elements could be further reduced to 0.2%. In detail the number of elements for the Sub-FF, FF-M and FF-L are listed in Table 1.

Figure 15 Modal analysis results of the FF-L assembly with constrained attachment points indicated via green triangles



Notes: (a) Mode 1, $f = 48$ Hz; (b) Mode 2, $f = 54$ Hz; (c) Mode 3, $f = 70$ Hz; (d) Mode 4, $f = 85$ Hz

Table 1 Resource overview of the Sub-FF, FF-M and FF-L

Name	Number of lattice core elements			Dimensions in mm			Boundary box in cm ³	Memory space in MB	Costs in (%)
	Hexa20	Penta15	Total	x	y	z			
Sub-FF	3266	160	3426	390	252	53	5209	358	5
FF-M	4228	18	4246	563	519	227	66329	1678	30
FF-L	11546	264	11810	587	476	414	115677	2785	100

Due to the volume size of the components boundary box and high number of lattice cells the faceting in the STL file lead to a large number of output files for the manufacturing process. The slicing and build job preparation of such big sets of data was challenging. Table 1 presents an overview of the data volume in megabytes (MB) required of the STL output data. A maximum of 2,785 MB were needed to process the FF-L in the STL data format. The volume of the FF-M boundary box was around half of the FF-L and the number of lattice cells were just under a third of the FF-L. The volume of the boundary box of the FF-M was 57% compared to the FF-L and contained 64% less lattice cells than the FF-L. Therefore, the memory space used for the FF-M required 40% less than for the FF-L. The costs of the FF-M was only a third of the costs of the FF-L. The Sub-FF had 71% less lattice cells than the FF-L. The volume of the boundary box of the Sub-FF was only 4.5% of the FF-L. Therefore, the memory space was only 12% of the memory space needed for the FF-L.

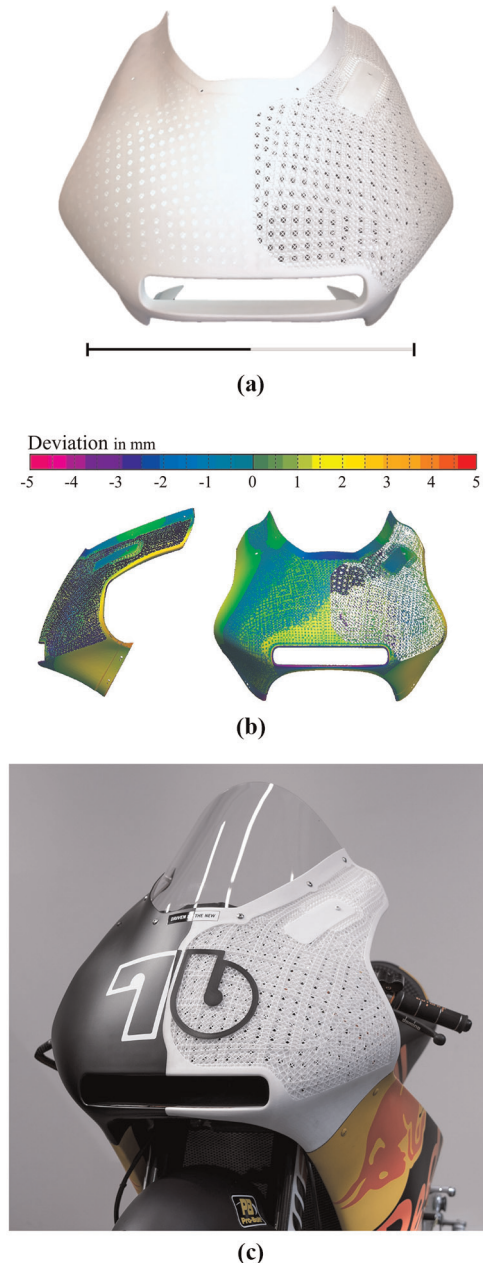
In Figure 16(a), the entire component FF-M has been laser sintered as a single part in a P770. The backlit picture, Figure 16(a), indicated that sufficient powder removal was possible.

The comparison of 3 D scan and CAD data of the FF-M in Figure 16(b) shows a dimensional accuracy in the windscreen area of -0.5 – 0.5 mm. At the mounting points for the side fairing the warpage was up to 2 mm. The lower edge of the air intake was warped downwards by 3.5 mm. The uppermost corner at the windscreen connection was warped downwards by 2.8 mm. Locally free areas of the side fairing connection displayed a local warpage of up to 5 mm. In the region where the top face sheet was removed to allow view onto the lattice core, the scan system was not capable of seamlessly reconstructing the geometry. This is likely related to the complexity of the structure, consisting of a network of very thin and overlapping trusses. Nevertheless, the dimensional accuracy of FF-M lead to a direct installation on an racing motorcycle without any further rework than finishing, see Figure 16(c).

4. Discussion

4.1 Design, simulation and testing of the Sub-FF

The basis of the design was a standard CAD data set, whereas the core volume was designed in consideration of the hexahedral meshing. Therefore, it was possible to divide the component into grid cells and solid material. This design approach demonstrates that different types of lattice structures can be combined with each other and reinforcement surfaces can be added to the core. It was shown that this methodology is not only suitable to design small 3PB bodies (Marshall *et al.*, 2020), but also applicable to a complex demonstrator such as a FF. The methodology is

Figure 16 Singular built full scale front fairing

Notes: (a) A single part of FF-M demonstrator produced with a P770 (scale bar 400 mm); (b) Build deviation comparison of FF-M between CAD and LS component; (c) Demonstrator of FF-M mounted on a full scale racing motorcycle

transferable to design large thin-walled lattice filled components.

Regarding the FE-model it was of great importance that the material properties were mapped (Sindinger *et al.*, 2020a, 2020b) on the surface structures. The RVEs of the lattice core were provided with corresponding thin-walled material characteristics (Tasch *et al.*, 2018). Additionally, the Sub-FF were produced with LS process parameters optimized for lattice structures. Geometrical and contact non-linear calculations were performed to satisfy the non-linearity in the experiment. Material non-linearity and buckling of cells including their failure behavior were not taken into account, as the focus was on the linear elastic behavior of the Sub-FFs. However, it was demonstrated that mapping of material properties for the surface structures has further increased the accuracy of the simulation compared to testing, whereby the stiffness deviation was only -6.5% at 1 mm and -9% at 5 mm deflection. Further improvements to the accuracy of the FE model could be achieved by introducing a higher k -value for the truss lattice cells. In addition the k -means clustering could be applied to the stringer and the sP cell property increasing the single property to multiple properties. Higher k -values result in a greater number of different unit cells, needing to be evaluated using FH. Therefore, the k -value chosen is a tradeoff in calculation time to accuracy.

The von Mises strain pattern of the Sub-FFs in the test and the FEA model appear very similar. However, a non-homogeneous strain jump appeared in the pattern at the strain peak areas of the FEA model. This could be due to the stiffness jump based on the freeze contact modeling between the lattice core elements and tetrahedron elements of the mounting area.

In the *FEA C* and the *FEA M* the tfs and bfs shell elements were connected to the core elements via coincident nodes. If the core enclosing volume gets geometrically more complex an approach with solid continuum elements could be more appropriate. However, the issue of defining the contact formulation has to be investigated. In addition, the material property mapping is still limited to shell elements. A comparison of the two approaches could be a starting point for further scientific research.

In the presented approach, the components have been meshed manually. The selection of the types of lattice cells was based on the specific stiffness properties (Marschall *et al.*, 2020). At areas of high curvature, the lattice cells penetrated the printed boundary surfaces of the tfs or bfs of the FF-L. Accordingly, these areas have to be cross-linked with smaller elements or no elements at all. An approach by splitting large hexahedrons into small hexahedrons is presented by Harris *et al.* (2004).

4.2 Lattice parameter optimization and part production

For the parameter optimization a lattice cuboid was designed and used in two different positions in four sequential build jobs by a trial-and-error approach. Based on the results it was possible to adapt the default parameter for PA12 into a sustainable parameter set for lattice structures. Key adjustments were done in the contour offset, z -compensation

and the angle-based z -compensation. A slight adaptation of the edge speed delivered near-contour trusses.

With the selected orientation of the S -, L - and X -trusses in the upright position, Figure 3(a), the process parameters could be adjusted in a step-wise manner. The 45° rotated position [as shown in Figure 3(b)] was used to investigate a more realistic representation of the truss distribution of real components in the build area. The caliper gauge was sufficiently accurate to investigate the dimensions of the lattice trusses.

The default process parameter delivered cross sections of the trusses between 0.5 and 1.0 mm. Especially for wall thicknesses between 0.6 and 2 mm the Young's modulus is strongly dependent on its wall thickness. The stiffness of the RVEs was based on the Young's modulus obtained in tensile tests of 0.8 mm thick tests specimens. Therefore, it was important to develop a process parameter for the lattice structures that ensured dimensional accuracy. Thus, it could be guaranteed that a comparison between FEA and demonstrator test generates reliable results.

Despite the different powder composition of virgin and aged powder, it was possible to transfer the optimized process parameter (3Q/T and 4X) from *P396* to *P770*. The complex geometry of the Sub-FF in *P396* and the FF-M in *P770* were successfully manufactured with similar dimensional accuracy. While the results were sufficient, it should be stated that conducting the entire parameter optimization on the *P770* machine could have provided an even better outcome for the FF-M. This, however, was within the scope of this study not possible due to the particularly high build job costs of the larger system.

The scan data depicted in Figure 12(a) to Figure 12(c) and Figure 16(b), revealed that in the relevant mounting areas of both, the Sub-FF as well as FF-M, the produced warpage was below 3 mm. This is acceptable for such structures, because the respective component can be bent to fit during assembly. The Sub-FF, produced at 42 mm height of the build volume displayed the lowest warpage. This might be related to a lower temperature gradient during the production process and during the unpacking process. However, the masses and stiffnesses were very close to each other with a maximum of 1.3% and 3.3% deviation, respectively. The 3D scan system was not able to scan dimensions of the bars on the FF-M, therefore, the measurements were carried out with the caliper gauge.

The transmitted light examination of the tested fairings exhibited good powder removal capabilities of the chosen design, but there was still residual powder around the sP lattice cells in the Sub-FF. The residual powder is very likely one of the reasons why the mass and stiffness of the tested Sub-FF was 7%–9% higher than in the FEA. With bigger lattice cells sizes ($10 \times 10 \times 5 \text{ mm}^3$) and holes up to 8 mm the cleaning of residual powder could be strongly improved for the FF-M. The hole pattern still corresponds to a very traditional thinking pattern to open closed structures. A more detailed perforation investigation would reveal further potential of such laser sintered structures.

The required memory space of the listed components in Table 1 was very high, therefore, the introduction of the angle-based z -compensation led to an enormously high pre-processing

effort in the preparation of the build job. The required memory space indicated that research is still necessary to reduce the STL faceting to achieve a faster processability.

5. Conclusion

In this study, the FE-mesh based design method (Marshall et al., 2020) was used to create a segment of a racing motorcycle front fairing and full scale single front fairing as an application-oriented demonstrator.

The layout of this study successfully demonstrated the possibility to predict the stiffness of non-periodic PA12 sandwich structures in margin of error of -7% or -9% depending on deflection position. Therefore, two FEA approaches were validated with three laser sintered geometrical complex test specimens (Sub-FF). All test specimens were built with an optimized parameter setup. In a first simulation approach (FEA C) constant material properties of PA12 per thickness were used and in a second approach (FEA M) transversely isotropic, thickness and orientation depended material properties were taken into account for every element of the top and bottom face sheet. In addition, the stiffness of the RVEs for truss- and surface-based non-periodic lattice cells was forward homogenized with the based on Young's modulus obtained by tensile test specimens of 0.8 mm wall thickness. Therefore, the process parameter optimization was essential to maintain a constant cross section of the lattice trusses. To increase the lightweight potential of the presented design approach, structural optimization algorithms should be developed to adapt the stiffness of the FH lattice cells to a load profile.

For application purposes a modal analysis of a racing motorcycle front fairing FF-L was carried out. The mounted FF-M demonstrator displays that it was possible to generate a lattice parameter on a P396 LS system and to transfer the parameter set onto a P770 including a successful fairing production.

For even larger components, such as the side fairings, it is necessary to divide them into smaller partial components. The number of cutouts and mounting brackets must be increased for such a structure. Therefore, future work should improve the usability of the workflow, consider a connection concept and reduce the required storage space of the STL data.

References

Breuninger, J., Becker, R., Wolf, A., Rommel, S. and Verl, A. (2012), *Generative Fertigung Mit Kunststoffen: Konzeption Und Konstruktion Für Selektives Lasersintern*, Springer, Berlin and Heidelberg.

Caulfield, B., McHugh, P.E. and Lohfeld, S. (2007), "Dependence of mechanical properties of polyamide components on build parameters in the SLS process", *Journal of Materials Processing Technology*, Vol. 182 Nos 1/3, pp. 477-488.

Feng, J., Fu, J., Lin, Z., Shang, C. and Li, B. (2018), "A review of the design methods of complex topology structures for 3D printing", *Visual Computing for Industry, Biomedicine, and Art*, Vol. 1 No. 1, p. 5.

Fish, J. (2014), *Practical Multiscaling*, John Wiley & Sons, Chichester.

Gibson, L.J. and Ashby, M.F. (1999), *Cellular Solids: structure and Properties*, 2nd ed., Cambridge University Press, Cambridge.

Goodridge, R.D., Tuck, C.J. and Hague, R. (2012), "Laser sintering of polyamides and other polymers", *Progress in Materials Science*, Vol. 57 No. 2, pp. 229-267.

Gorguluarslan, R.M., Park, S.-I., Rosen, D.W. and Choi, S.-K. (2015), "A multilevel upscaling method for material characterization of additively manufactured part under uncertainties", *Journal of Mechanical Design*, Vol. 137 No. 11.

Harris, N.J., Benzley, S.E. and Owen, S.J. (2004), "Conformal refinement of all-hexahedral element meshes based on multiple twist plane insertion", *IMR*, pp. 157-168.

Lynch, M.E., Mordasky, M., Cheng, L. and To, A. (2018), "Design, testing, and mechanical behavior of additively manufactured casing with optimized lattice structure", *Additive Manufacturing*, Vol. 22, pp. 462-471.

Maconachie, T., Leary, M., Lozanovski, B., Zhang, X., Qian, M., Faruque, O. and Brandt, M. (2019), "SLM lattice structures: properties, performance, applications and challenges", *Materials & Design*, Vol. 183, p. 108137.

Marshall, D., Rippl, H., Ehrhart, F. and Schagerl, M. (2020), "Boundary conformal design of laser sintered sandwich cores and simulation of graded lattice cells using a forward homogenization approach", *Materials & Design*, Vol. 190, p. 108539.

Na, S., Xumin, L. and Yong, G. (2010), "Research on k-means clustering algorithm: an improved k-means clustering algorithm", *2010 Third International Symposium on Intelligent Information Technology and Security Informatics*, pp. 63-67.

Park, S.-I. and Rosen, D.W. (2018), "Homogenization of mechanical properties for material extrusion periodic lattice structures considering joint stiffening effects", *Journal of Mechanical Design*, Vol. 140 No. 11.

Rosen, D.W. (2007), "Computer-aided design for additive manufacturing of cellular structures", *Computer-Aided Design and Applications*, Vol. 4 No. 5, pp. 585-594.

Sindinger, S.-L., Kralovec, C., Tasch, D. and Schagerl, M. (2020a), "Thickness dependent anisotropy of mechanical properties and inhomogeneous porosity characteristics in laser-sintered polyamide 12 specimens", *Additive Manufacturing*, Vol. 33, p. 101141.

Sindinger, S.-L., Marschall, D., Kralovec, C. and Schagerl, M. (2021), "Material modelling and property mapping for structural FEA of thin-walled additively manufactured components", *Virtual and Physical Prototyping*, Vol. 16 No. 1, pp. 97-112.

Sindinger, S.-L., Marschall, D., Kralovec, C. and Schagerl, M. (2021), "Structural response prediction of thin-walled additively manufactured parts considering orthotropy", *Thickness Dependency and Scatter, Materials*, Vol. 14 No. 9.

Tasch, D., Mad, A., Stadlbauer, R. and Schagerl, M. (2018), "Thickness dependency of mechanical properties of laser-sintered polyamide lightweight structures", *Additive Manufacturing*, Vol. 23, pp. 25-33.

Weeger, O., Boddeti, N., Yeung, S.-K., Kaijima, S. and Dunn, M. (2019), “Digital design and nonlinear simulation for additive manufacturing of soft lattice structures”, *Additive Manufacturing*, Vol. 25, pp. 39–49.

Yuan, Z. and Fish, J. (2008), “Toward realization of computational homogenization in practice”, *International*

Journal for Numerical Methods in Engineering, Vol. 73 No. 3, pp. 361–380.

Corresponding author

Sigfrid-Laurin Sindinger can be contacted at: sigfrid-laurin.sindinger@jku.at

For instructions on how to order reprints of this article, please visit our website:

www.emeraldgroupublishing.com/licensing/reprints.htm

Or contact us for further details: **permissions@emeraldinsight.com**